Flow Turbulence Combust (2014) 92:429–449
DOI 10.1007/s10494-013-9471-y

Experimental and Numerical Study of the Scalar Turbulent/Non-Turbulent Interface Layer in a Jet Flow

M. Gampert · K. Kleinheinz · N. Peters · H. Pitsch

Received: 15 December 2012 / Accepted: 7 May 2013 / Published online: 26 June 2013

Abstract Based on two large-eddy simulations (LES) of a non-reacting turbulent round jet with a nozzle based Reynolds number of 8,610 with the same configuration as the one that has recently been investigated experimentally (Gampert et al., 2012; J Fluid Mech, 2012; J Fluid Mech 724:337, 2013), we examine the scalar turbulent/non-turbulent (T/NT) interface layer in the mixture fraction field of the jet flow between ten and thirty nozzle diameters downstream. To this end, the LES—one with a coarse grid and one with a fine grid—are in a first step validated against the experimental data using the axial decay of the mean velocity and the mean mixture fraction as well as based on radial self-similar profiles of mean and root mean square values of these two quantities. Then, probability density functions (pdf) of the mixture fraction at various axial and radial positions are compared and the quality of the LES is discussed. In general, the LES results are consistent with the experimental data. However, in the flow region where the imprint of the T/NT interface layer is dominant in the mixture fraction pdf, discrepancies are observed. In a next step, statistics of the T/NT interface layer are studied, where a satisfactory agreement for the pdf of the location of the interface layer from the higher resolved LES with the experimental data is observed, while the one with the coarse grid exhibits considerable deviations. Finally, the mixture fraction profile across the interface is investigated where the same trend as for the pdf of the location is present. In particular, it is found that the sharp interface that is present in experimental studies (Gampert et al., J Fluid Mech, 2012; Westerweel et al., J Fluid Mech 631:199, 2009) is less distinct in the LES results and rather diffused in radial direction outside of the T/NT interface layer.

Keywords Turbulent/non-turbulent interface layer · Mixture fraction pdf · Jet flow · Large-eddy simulation · Rayleigh scattering

M. Gampert (✉) · K. Kleinheinz · N. Peters · H. Pitsch
Institute for Combustion Technology, RWTH Aachen University,
Templergraben 64, 52056 Aachen, Germany
e-mail: m.gampert@itv.rwth-aachen.de

1 Introduction

Turbulence tends to be created locally where the flow is most unstable, which can be observed for instance in jet flows, wakes and boundary layers, cf. [5, 6]. In these examples turbulent regions are located adjacent to non-turbulent (NT) ones, where no turbulence is generated. Such intermittent regions are also reported for thermal convection, where locally regions of high turbulence intensity are next to regions with much lower intensity, cf. [7, 8]. Townsend [9, 10] quantified this behavior in terms of an intermittency factor γ, defined as the fraction of the signal that is turbulent. Corrsin and Kistler [11] first termed the layer separating the turbulent from the non-turbulent (T/NT) region as the 'laminar superlayer'. Bisset et al. [5] note that irrotational velocity fluctuations are usually found in the non-turbulent flow outside the interface layer, which does not mark an absence of velocity fluctuations but a change in the character of the fluctuations from vortical to irrotational. Since vorticity is transmitted to fluid only through the action of molecular viscosity, there must exist a shear layer that is essentially viscous in nature, though it may be extremely thin. Across this thin layer of turbulent fluid, all major changes between outer fluid and the fully turbulent interior fluid take place, including those of a transported scalar.

In combination with the detection of so-called coherent structures in various types of turbulent flows, cf. [12–16], the question arises how the local topology of these flows may be described from a structural point of view and how their impact may be described physically and quantified in terms of turbulence statistics. Townsend [8, 17, 18] was the first to bring forth the idea of describing so called coherent eddies from two-point correlations, cf. [19]. Recently, Marusic and Adrian [20] gave a more precise definition of these coherent structures and the observed organized motion. Following the investigations of [21–23], Philip and Marusic [6] used a random collection of coherent large-scale eddies to describe first and second order statistics in axisymmetric jets and wakes. The latter authors further investigate the physical importance of these large-scale eddies in the local entrainment process that describes the advancement of the T/NT interface layer into the irrotational fluid normal to its own surface, cf. [5]. While Liepmann and Gharib [15] and Yoda et al. [24] discuss the impact of these large-scale eddies and the motion of large-scale vortices (engulfment) on the entrainment process, Westerweel et al. [4, 25] and Mathew and Basu [26] suggest that small-scale eddy motions (nibbling) acting on the T/NT interface layer are the dominant physical mechanism.

These nibbling eddies are of major importance for the dynamics of the interface layer, see Hunt et al. [27] for a review of recent investigations. Detailed spatial analyses of this region have recently been made experimentally, cf. [4, 28–30], and numerically, cf. [31–33], giving deeper insight into the vorticity dynamics close to the T/NT interface layer. In addition, Westerweel et al. [34] examined the temperature field of a non-isothermal jet and observed good agreement of the statistics with those obtained from investigations of concentration and axial momentum, see [4, 25, 29, 31, 35]. Furthermore, da Silva and Pereira [31] argue, based on scaling arguments involving the viscosity and the rate of strain that in the presence of a mean shear, the characteristic length scale δ associated with the thickness of the interface layer scales with the Taylor microscale λ.

In terms of combustion in a non-premixed system, the region of the T/NT interface layer is also of major importance as combustion occurs in the vicinity of the stoichiometric mixture fraction Z_{st}. The value of the latter is about 0.06 for different hydrocarbon/air mixtures and is defined as the mass fraction of fuel stream in a given fuel-air mixture. In a jet flame, owing to the very low values of stoichiometric mixture fraction, combustion occurs in the outer boundary at lower mixture fraction values of the turbulent fuel jet, which is characterized by turbulent regions (of fuel) adjacent to non-turbulent regions (of air). These two regions are thus separated by a T/NT interface layer.

In a previous work, cf. [2], the contribution of the T/NT interface layer to the mixture fraction probability density function (pdf) P(Z) at various axial and radial locations has been examined and the composite model proposed by Effelsberg and Peters [36] for the mixture fraction pdf in non-premixed combustion has been used. Thereby, the structure of the scalar T/NT interface layer in this free shear flow has been identified and it was concluded that the T/NT interface and its contributions to the mixture fraction pdf are of major importance particularly in the early part of the jet. Furthermore, statistics such as the pdf of the location of the T/NT interface layer and the scalar profile across the latter were investigated and found to be in good agreement with literature data, cf. [4]. In addition, the scaling of the thickness δ of the scalar T/NT interface layer was analyzed at Reynolds numbers $Re_\lambda = 60 - 140$, where Re_λ denotes the local Reynolds number based on the Taylor scale λ, using the mixture fraction profile in interface normal direction. It was observed that $\delta/L \propto Re_\lambda^{-1}$, where L is an integral length scale, meaning that $\delta \propto \lambda$.

The region of the T/NT interface layer was recently further analyzed by Mellado et al. [37], who investigated the DNS of a temporally evolving shear layer using gradient trajectories. Based on these gradient trajectories, they partition the scalar field into a fully turbulent zone, a zone containing the T/NT interface layer and the outer laminar flow. Based on the different regions, they examine the probability of these three zones at different locations in the shear layer and investigate the scalar probability density function and the conditional scalar dissipation rate in the zones in the presence of external intermittency. This approach was adopted by Gampert et al. [1], where zonal statistics of the scalar pdf $P(Z)$ as well as the scalar difference along a scalar gradient trajectory ΔZ and its mean scalar value Z_m were examined based on experimentally obtained scalar fields in a jet flow. In addition, Gampert et al. [1] reconstruct the scalar probability density function $P(Z)$ from zonal gradient trajectory statistics of the joint probability density function $P(Z_m, \Delta Z)$ and observe a very good qualitative and quantitative agreement with the experimental data.

Relating the above described results to the widely used RANS simulations, we note that the standard models for $\langle Z \rangle$ and $\langle Z'^2 \rangle$ are only valid in the limit of infinitely large Reynolds number and do not account for molecular transport in the T/NT interface. Thus, the physics of this layer are not included in such a simulation and cannot be captured even if the RANS equations were extended to higher order moments. Consequently, one would have to derive additional model equations if the physics of the T/NT interface layer that is inherent to free shear flows were to be predicted by a RANS code. This is different for the case of a large-eddy simulation (LES) as here on the one hand diffusive processes are included for the resolved scales and on the other hand the diffusive terms including the unresolved sub-grid scales are

modeled. A T/NT interface layer is hence expected to be present also in LES of free shear flows. However, it is unknown if the physics and their impact on the statistics, such as for instance the mixture fraction pdf, is properly reproduced.

Therefore, the T/NT interface layer is investigated in the present study based on two LES of a jet flow with the same characteristics as the one examined experimentally by Gampert et al. [2]. In section two, we briefly recall the experimental investigation that is used as a reference data base in the following. In section three, the LES is presented and validated in terms of axial decay of the mean velocity and the mean scalar along the jet axis as well as based on radial profiles of mean and root mean square (r.m.s.) values. The LES data is then employed in section four to study in a first step the mixture fraction pdf from simulation and experiment at various axial and radial locations. In a second step, we examine statistics of the T/NT interface layer, where in particular the location of the interface and the scalar profile across the latter are of interest. Finally, the paper is concluded with a brief summary in section five.

2 Experiment

The experimental arrangement has already been described and validated to some extent in companion papers, cf. [1, 2] (Gampert et al. 2013, Scalar gradient trajectory measurements using high-frequency cinematographic planar rayleigh scattering, submitted), so that only a brief description is given in the following.

The experiments were performed in a coflowing turbulent jet facility. The facility consists of a center steel tube with an inner nozzle diameter d = 12 mm. The surrounding coflow tube had a diameter of 150 mm, which was large enough to reduce the experimental setup to a two-stream mixing problem. Research grade propane (99.95 % pure) was fed through the center tube using a mass flow controller (OMEGA FMA-2600A) at a flow rate to achieve a jet exit velocity of $U_0 = 3.30$ m/s, resulting in a jet exit Reynolds number of $Re_0 = 8{,}610$. The coflow gas was chosen as carbon dioxide owing to its larger Rayleigh cross-section compared to air, which was necessary to obtain an accurate determination of the scalar T/NT interface layer. The mean velocity of the CO_2 coflow was 0.05 m/s, as determined from laser Doppler anemometry (LDA) measurements. The different experimental parameters are shown in Table 1.

For the velocity measurements that are discussed in the following, an LDA system, i.e. a Coherent Innova 300 laser coupled to a one-component fiber optic of Aerometrics Inc. was used. In the present case, small glass spheres with a diameter

Table 1 Experimental parameters

x/d	10	15	20	30
Jet exit velocity U_0 [m/s]	3.30	3.30	3.30	3.30
Mean centerline velocity U_C [m/s]	1.91	1.32	1.01	0.65
Mean centerline mixture fraction Z_C	0.37	0.25	0.19	0.14
Kolmogorov scale η [mm]	0.09	0.12	0.16	0.24
Taylor scale λ [mm]	1.65	2.20	3.16	4.61
Nozzle based Reynolds number Re_0	8,610	8,610	8,610	8,610
Taylor based Reynolds number Re_λ	89	91	96	96

between 3.5–7 μm were used as tracer particles. Two beams, with wavelengths of 488 and 514 nm, were passed through a Bragg cell which resulted in two more beams whose frequency was offset by 40 kHz from the input wavelengths. These beams were focused to a spot, approximately 100 μm diameter, using a biconvex lens (f.l.=300 mm). The Doppler signals were focused by another biconvex lens (f.l.=300 mm) to the detector. The two velocity components were computed using the data-processing software Real-Time Signal Analyzer provided by Aerometrics Inc.

High-speed (kHz-rate) two-dimensional Rayleigh scattering imaging was performed in the y-z-plane, normal to the bulk flow direction x, at downstream locations x/d = 10–30, Fig. 1 shows the schematic of the experimental setup. The high repetition-rate imaging enabled us to account for the orientation of the scalar T/NT interface, cf. [2], while computing topological statistics. Two frequency doubled beams ($\lambda = 527$ nm) from a high-frequency dual-head Nd:YLF laser (Litron Lasers LDY303HE-PIV) were made coincident, both spatially and temporally, to deliver a total energy of about 32 mJ/pulse at 1 kHz (32 W). To account for laser energy fluctuations, the signal is corrected on a shot by shot basis by a 12bit energy monitor (LaVision Online Energy Monitor). The polarization of both of the beams was normal to the jet axis; this maximized the Rayleigh scattering signals in the imaging plane. The beams were transformed into a horizontal collimated sheet using a combination of a spherical and a cylindrical lens. The width and the thickness of the resultant sheet were approximately 10 mm and 0.3 mm respectively. Images were acquired at 1 kHz using a high-speed CMOS camera (LaVision HighSpeedStar 6, 1×1 k pixels) fitted with a camera lens (Nikon f.l.=85 mm) stopped at $f/1.4$. An extension ring was placed between the camera and the lens to minimize the working distance; the resulting field of view was about 60×60 mm.

The Rayleigh scattering images were corrected for background scattering, camera dark noise and laser-sheet inhomogeneities. For calibration purposes, measurements of pure propane ($Z = 1$) and CO_2 ($Z = 0$), respectively, have been performed. Based on these, the mixture fraction was then determined from the measured mole-fraction using linear interpolation. The signal-to noise ratio (SNR) of the raw images

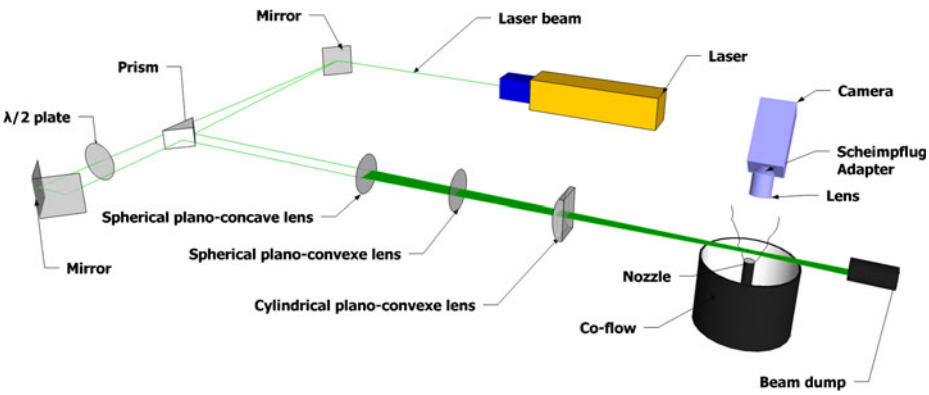

Fig. 1 Experimental setup for the high-speed Rayleigh scattering measurements

was about 20 in the pure CO_2 region and about 40 in the pure propane region. The time interval between the successive images was 1 ms.

3 Large-Eddy Simulation

In this section, the details of the simulation are presented. In the first subsection the details of the LES, including the mathematical and numerical framework, are described. In the second and third subsection the velocity and scalar profiles are validated.

3.1 Details of the simulations

The LES of the non-reacting turbulent round jet are conducted using a parallel finite difference code [38]. The code solves the filtered Navier-Stokes equations in the low Mach limit

$$\frac{\partial}{\partial t}\left(\overline{\rho}\right) + \frac{\partial}{\partial x_j}\left(\overline{\rho}\widetilde{u}_j\right) = 0, \tag{1}$$

$$\frac{\partial}{\partial t}\left(\overline{\rho}\widetilde{u}_i\right) + \frac{\partial}{\partial x_j}\left(\overline{\rho}\widetilde{u}_i\widetilde{u}_j\right) = -\frac{\partial}{\partial x_i}\left(\overline{p}\right) + \frac{\partial}{\partial x_j}\left(\overline{\sigma}_{ij}\right) + \frac{\partial}{\partial x_j}\left(\overline{\sigma}_{ij,sfs}\right), \tag{2}$$

where $\overline{\rho}$ denotes the filtered density and $\widetilde{u}_i$ is the filtered velocity. Due to the equal molecular weight of propane and CO_2 the density is constant throughout the whole domain. The $\overline{(\cdot)}$ and $\widetilde{(\cdot)}$ operators denote spatial filtering and spatial density weighted filtering, respectively. The viscous stress tensor $\overline{\sigma}_{ij}$ in the momentum equation reads

$$\overline{\sigma}_{ij} = 2\overline{\rho\nu}\left[\widetilde{S}_{ij} - \frac{1}{3}\delta_{ij}\frac{\partial}{\partial x_k}(\widetilde{u}_k)\right], \tag{3}$$

where the rate of strain tensor is defined as

$$\widetilde{S}_{ij} = \frac{1}{2}\left[\frac{\partial}{\partial x_j}(\widetilde{u}_i) + \frac{\partial}{\partial x_i}(\widetilde{u}_j)\right]. \tag{4}$$

The term $\overline{\sigma}_{ij,sfs}$ in Eq. 2 denotes the subfilter stress

$$\overline{\sigma}_{ij,sfs} = \overline{\rho}\widetilde{u}_i\widetilde{u}_j - \overline{\rho}\widetilde{u_i u_j}. \tag{5}$$

This term is unclosed and thus has to be modeled, which is achieved by employing a dynamic Smagorinsky-type model with Lagrangian filtering [39, 40]. In the low Mach limit, the pressure variable $\overline{p}$ must be determined in such a way that it leads to a continuity-satisfying momentum solution [41]. A multi-grid HYPRE solver is used for the Poisson equation of the pressure [42].

For the filtered mixture fraction $\widetilde{Z}$ the following transport equation is solved

$$\frac{\partial}{\partial t}\left(\overline{\rho}\widetilde{Z}\right) + \frac{\partial}{\partial x_j}\left(\overline{\rho}\widetilde{u}_j\widetilde{Z}\right) = \frac{\partial}{\partial x_j}\left(\overline{\rho}\widetilde{\mathcal{D}}_Z\frac{\partial}{\partial x_j}\widetilde{Z}\right) + \frac{\partial}{\partial x_j}\left(\overline{\Xi}_{jZ,sfs}\right). \tag{6}$$

The diffusivity $\mathcal{D}_Z$ is fixed to match the molecular diffusivity of propane in CO_2 as in the experiment. The term $\overline{\Xi}_{jZ,sfs}$ denotes the subfilter scalar flux

$$\overline{\Xi}_{jk,sfs} = \overline{\rho}\widetilde{\phi_k}\widetilde{u}_j - \overline{\rho}\widetilde{\phi_k u}_j, \tag{7}$$

which is unclosed. A dynamic Smagorinsky-type model with Lagrangian filtering is employed to calculate the turbulent diffusivity, which is used to close the subfilter scalar flux [43].

The code uses a Crank-Nicholson type time advancement, and an iterative predictor-corrector updating scheme. Velocity gradients are determined using second order schemes, while scalar gradients are calculated based on a third order WENO [44] finite difference scheme. To increase the accuracy of spatial and temporal discretization a staggered-variable formulation is employed in the code [38].

The LES are carried out on two different meshes to assess the influence of the grid resolution on the T/NT interface layer. The numerical domain is discretized by a structured mesh with cylindrical coordinates. The coarse mesh consists of 1.5 million grid cells, which are distributed with $256 \times 96 \times 64$ grid cells in axial, radial and circumferential direction, respectively. The fine mesh consists of 3.1 million grid cells, with the count of grid cells equal to the coarse mesh in axial and circumferential direction. In radial direction the number of grid points is doubled to increase the resolution of the T/NT interface layer so that the grid consists of $256 \times 192 \times 64$ grid cells. The numerical domain extends from $x/d = -1$ upstream of the jet (a small portion of the inlet nozzle geometry is included) to $x/d = 50$ downstream of the nozzle exit in axial direction and extends to a radius of r/d=33 in radial direction.

Both meshes are uniform in the center region and stretched in axial and radial direction downstream in axial direction and towards larger radii. This allows a high resolution close to the nozzle and in the region of the T/NT interface layer in the area of the measurements ($x/d = 10$–30). Figure 2 shows the instantaneous axial velocity on the fine grid and Fig. 3 displays an instantaneous snapshot of the mixture fraction field on the fine grid. In both figures the locations of the measurement planes at $x/d = 10$, $x/d = 15$, $x/d = 20$, and $x/d = 30$ are marked by solid white lines.

Table 2 shows the ratio of the filter width to the Kolmogorov scale for both meshes. In the area of the measurement planes this ratio varies from 12 to 25 and 9 to 23 for the coarse grid and the fine grid, respectively. The filter ratio is smaller for the fine grid due to the higher number of grid points in radial direction. At the

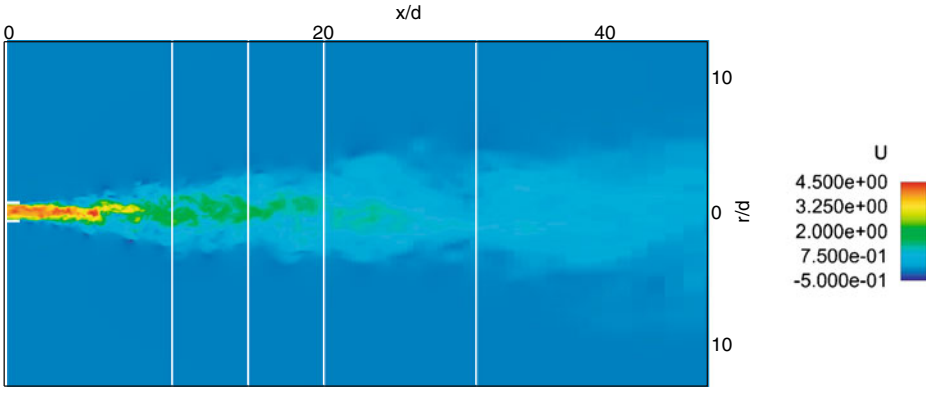

Fig. 2 Illustration of the instantaneous velocity field in streamwise direction for the fine LES. For clarity only a small part of the domain is shown. *White vertical lines* indicate measurement planes at $x/d = 10$, 15, 20, and 30, from *left* to *right*

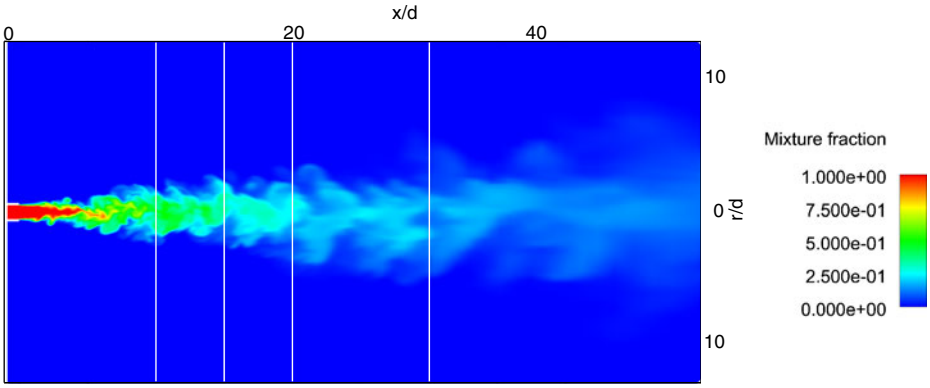

Fig. 3 Illustration of the instantaneous mixture fraction field for the fine LES. For clarity only a small part of the domain is shown. White vertical lines indicate measurement planes at x/d = 10, 15, 20, and 30, from *left* to *right*

centerline, the ratio of the radial grid spacing to the axial grid spacing is 0.5 for the coarse grid and 0.25 for the fine grid. Due to the definition of the filter width

$$\Delta = \sqrt{dx^2 + dr^2} \tag{8}$$

the additional cells of the fine grid reduce the filter width only by approximately 10 %. However, the resolution of the T/NT interface layer benefits from the additional grid points as will be discussed in the following.

The boundary conditions are set to match the experimental setup. To generate velocity data at the inlet of the numerical domain, an LES of the inflow pipe is conducted prior to the main LES. The resulting velocity data are prescribed as inlet condition to the main LES. For the mixture fraction at the inlet, a Dirichlet condition is used. At the outlet a convective outlet condition is imposed for the velocity and a no-flux condition for the scalar. For both velocity and scalar transport equations a no-flux condition is used at the outer radial boundary.

3.2 Profiles along the jet axis

In Fig. 4, the inverse of the mean centerline velocity U_c (mean centerline mixture fraction Z_c) over the value at the nozzle U_0 (Z_0) is plotted along the jet axis at the downstream locations presented in Tables 1 and 2. Note that here and in the following the subscript c denotes a quantity on the centerline, $\langle\cdot\rangle$ indicates an ensemble average in time at a fixed radial location, $\langle U\rangle$ is the mean and u the fluctuating

Table 2 Ratio of the filter width to the Kolmogorov scale Δ/η of the two LES meshes on the centerline of the domain

The filter width is defined as $\Delta = \sqrt{dx^2 + dr^2}$

x/d	Coarse grid	Fine grid
10	25	23
15	19	17
20	16	13
30	12	9

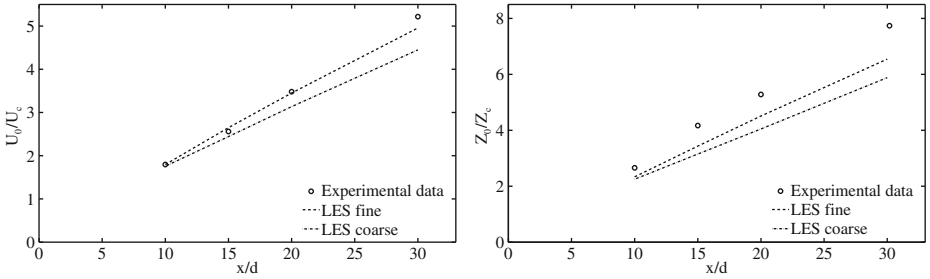

Fig. 4 Variation of the inverse of (**a**) the mean velocity and (**b**) the mean mixture fraction with the axial distance along the centerline from LES and experiment

component of the velocity. Furthermore, all figures in this section display the self similar profile, on which the LES data at the measurement planes collapses, for the LES data and the experimental data. For the sake of clarity, in this chapter only the parameters of the fine grid LES are discussed and compared to the experimental data (Gampert et al. 2013, Scalar gradient trajectory measurements using high-frequency cinematographic planar rayleigh scattering, submitted). Following results discussed in the literature [45], the mean axial velocity at the centerline follows x^{-1}. In order to determine the slope of the curves, we have fitted both computational results and experimental data the data to the expressions

$$\frac{U_c}{U_0} = k_u \left[\frac{d}{x - x_0} \right] \tag{9}$$

and

$$\frac{Z_c}{Z_0} = k_Z \left[\frac{d}{x - x_0} \right] \tag{10}$$

in which x_0 denotes the virtual origin of the jet. The fitted parameters are presented in Table 3 and compared to the experimental results (Gampert et al. 2013, Scalar gradient trajectory measurements using high-frequency cinematographic planar rayleigh scattering, submitted) as well as to literature data. We observe very good agreement

Table 3 LES, experimental and literature values for the parameters of Eqs. 8–11 together with the virtual origins of velocity and mixture fraction

	Fine grid LES	Experiment (Gampert et al. 2013, Scalar gradient trajectory measurements using high-frequency cinematographic planar rayleigh scattering, submitted)	Literature
k_u	6.4	6.1	6.1 [47], 6.2 [46]
$(x_0/d)_u$	−1.7	−3.2	−2.5 [46], −2.9 [47]
k_z	4.8	4.8	5.3 [46], 5.5 [48]
$(x_0/d)_z$	−1.3	−1.7	−0.9 [46]
K_u	73.7	77.5	75.2 [49], 76.1 [48], 77.4 [47]
K_Z	57.7	59.2	58.2 [46], 59.1 [48]

for the data of the fine grid LES with both the experimental values and literature data [46, 47]. The values for k_u and k_Z, which represent the inverse of the slope of the variation of the mean velocity and the mean mixture fraction in Fig. 4 are very close to the experimental values and literature data [46–48]. Also the computed virtual origin of the scalar is close to both the experimental value and literature data [46], whereas that of the velocity is slightly lower but well in the range of the experimental value and literature data [46, 47].

3.3 Radial profiles of mean and root mean square values of velocity and mixture fraction

In a next step, we examine the radial profiles of the mean $\langle U \rangle$, $\langle Z \rangle$ and r.m.s. $\langle u^2 \rangle^{1/2}$, $\langle Z'^2 \rangle^{1/2}$ of velocity and mixture fraction normalized by the respective mean value on the jet axis as a function of the non-dimensional similarity coordinate $\tilde{r} = r/(x - x_0)$. Figure 5a depicts the radial evolution of $\langle U \rangle / U_c$. The curve of the fine grid LES agrees very well with the experimental data, whereas there is a small offset of the coarse LES. We find an excellent collapse of all the mean quantities of the LES data on a unique curve, which is fitted to [46] (Gampert et al. 2013, Scalar gradient trajectory measurements using high-frequency cinematographic planar rayleigh scattering, submitted)

$$\frac{\langle U \rangle}{U_c} = \exp(-K_u \tilde{r}^2), \tag{11}$$

yielding a value of $K_u = 73.7$. This value is very close to the value found in the literature as well as the one of the experiment (cf. Table 3). In addition, the half-width radius $r_{1/2}$ of the mean velocity is found at $\tilde{r} = 0.09$ as compared to $\tilde{r} = 0.08$ obtained by Gampert et al. (2013, Scalar gradient trajectory measurements using high-frequency cinematographic planar rayleigh scattering, submitted).

Radial r.m.s. profiles of the velocity versus $\tilde{r}$ are presented in Fig. 5b. The profiles of the LES data at the different measurement locations collapse with a normalized peak magnitude of approximately $\langle u^2 \rangle^{1/2} / U_c = 0.25$ at $\tilde{r} = 0.04$, which is close to the values reported by Gampert et al. (2013, Scalar gradient trajectory measurements using high-frequency cinematographic planar rayleigh scattering, submitted) ($\langle u^2 \rangle^{1/2} / U_c = 0.255$ at $\tilde{r} = 0.045$) and Talbot et al. [46] ($\langle u^2 \rangle^{1/2} / U_c = 0.26$ at $\tilde{r} = 0.05$).

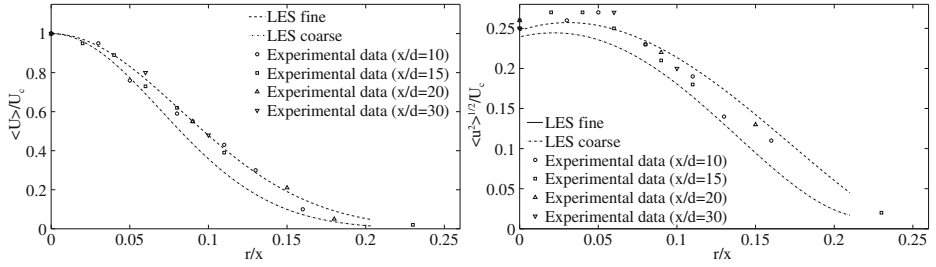

Fig. 5 Radial profiles for **a** mean value $\langle U \rangle / U_c$ and **b** r.m.s. value $\langle u^2 \rangle^{1/2} / U_c$

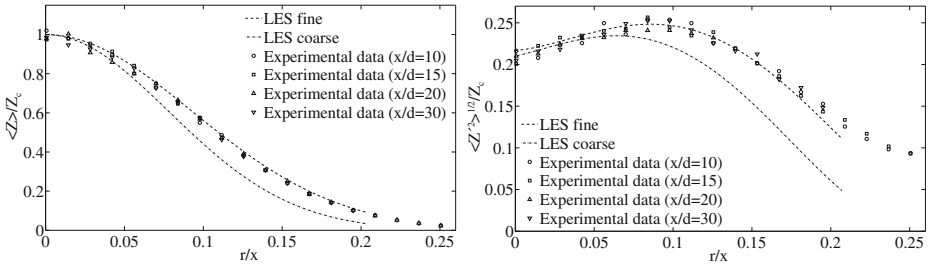

Fig. 6 Radial profiles for **a** mean value $\langle Z \rangle / Z_c$ and **b** r.m.s. value $\langle Z'^2 \rangle^{1/2} / Z_c$

Figure 6 shows the radial profiles for mixture fraction. Again, the curves of the fine grid LES agree very well with the experimental data for both the mean and the r.m.s. values, whereas the coarse grid LES shows an offset of approximately 15 % to the experimental data. The LES data of the radial evolution of the mixture fraction is fitted to

$$\frac{\langle Z \rangle}{Z_c} = \exp(-K_Z \tilde{r}^2). \tag{12}$$

The values of the parameter K_Z for the LES, the experiment and the literature, see Table 3, are in very good agreement. The half-width radius b_c of the mean mixture fraction is found at $\tilde{r} = 0.11$, which is in excellent agreement with (Gampert et al. 2013, Scalar gradient trajectory measurements using high-frequency cinematographic planar rayleigh scattering, submitted) ($\tilde{r} = 0.11$). Radial r.m.s. profiles of the mixture fraction versus $\tilde{r}$ are presented in Fig. 6b. The lines indicate fits of the respective LES data, which in this case represents a fourth-order polynomial

$$\frac{\langle Z'^2 \rangle^{1/2}}{Z_c} = p_0 + p_1 \tilde{r} + p_2 \tilde{r}^2 + p_3 \tilde{r}^3 + p_4 \tilde{r}^4, \tag{13}$$

with $p_0 = 0.22$, $p_1 = 0.18$, $p_2 = 10.6$, $p_3 = -119.2$, $p_4 = -251.4$. These values are close to the ones reported by [46, 50] (Gampert et al. 2013, Scalar gradient trajectory measurements using high-frequency cinematographic planar rayleigh scattering, submitted). Furthermore, we observe the normalized peak magnitude of approximately $\langle Z^2 \rangle^{1/2} / Z_c = 0.25$ at $\tilde{r} = 0.09$, which is in the range of values reported by [46, 50, 51] (Gampert et al. 2013, Scalar gradient trajectory measurements using high-frequency cinematographic planar rayleigh scattering, submitted).

4 Results and Discussion

In the course of this section, we will in a first step investigate and compare the mixture fraction pdfs obtained from the experimental study and from LES. Then, statistics of the scalar T/NT interface layer are investigated, where we examine the pdf of the location of the interface layer in radial direction as well as the scalar profile across the latter.

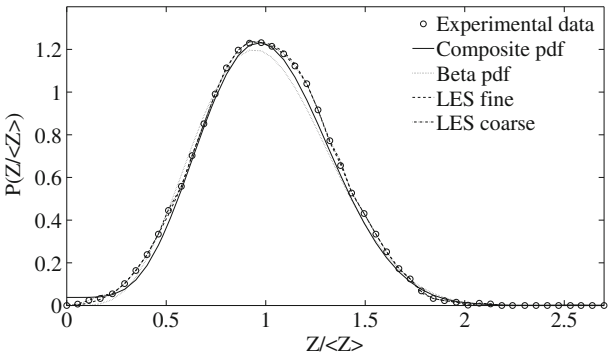

Fig. 7 Comparison of mixture fraction pdfs from LES, experiment and composite model at x/d = 15 and $\tilde{r} = 0$

4.1 The mixture fraction pdf in a jet flow

In the following, we will discuss the mixture fraction pdf in the jet at different axial and radial positions, computed from the two LES and compared to the experimental data in Figs. 7, 8, 9, 10, 11 and 12. To this end, a histogram of the instantaneous mixture fraction divided by the local mean mixture fraction $Z/\langle Z\rangle$ was made by sorting the data into bins. Then the histogram was normalized

$$\int_0^\infty P(Z/\langle Z\rangle)d(Z/\langle Z\rangle) = 1, \tag{14}$$

to form a pdf of the mixture fraction. $Z/\langle Z\rangle$ is chosen as the independent variable to remove the effect of downstream decay of the mean mixture fraction following for instance Lubbers et al. [48].

Physically, specific parts of the pdfs will be attributed to different regions of the scalar fields, that contain turbulent and non-turbulent regions as well as the T/NT interface layer. To this end, we will use the composite model of Effelsberg and Peters [36], which has recently been successfully validated for the mixture fraction pdf in a jet flow, cf. [2]. This model was chosen here, because its solution can easily be computed from the first four moments of the pdf and it provides the pdfs of different topological parts of the field. This model combines several parameters, which represent the fraction of the signal from the scalar T/NT interface layer, the

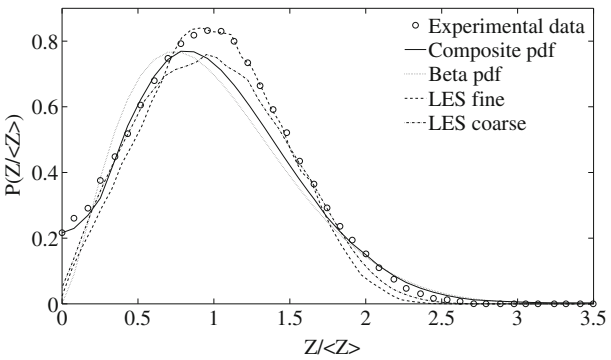

Fig. 8 Comparison of mixture fraction pdfs from LES, experiment and composite model at x/d = 15 and $\tilde{r} = 0.110$

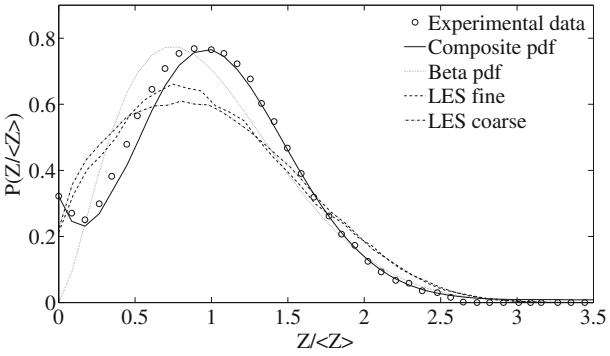

Fig. 9 Comparison of mixture fraction pdfs from LES, experiment and composite model at x/d = 15 and $\tilde{r} = 0.135$

presumed shape of the mixture fraction pdf within the interface layer and a β-pdf, see [36] for further details. These parameters are used to compute a composite pdf, which is shown in Figs. 7–12 for different locations. In addition, a β-pdf is included for comparison that has been calculated using the first two moments of the experimental pdf.

In Figs. 7 and 11, the pdfs on the centerline are shown at x/d = 15 and x/d = 20. We observe a shape that is approximately Gaussian and has a negligible contribution from the interface layer. Furthermore, the agreement of the β-pdf and the two LES cases with the measured pdf is excellent. This changes in Fig. 8 (x/d = 15), where the contribution from the T/NT interface layer is already noticeable. We observe a good agreement of the measured data with the better resolved LES. The LES with the coarse grid, however, has a lower peak value that is also slightly shifted to smaller mixture fraction values. However, both LES strongly underpredict the non-zero value of $P(Z/\langle Z\rangle)$ at the origin. This deviation is even stronger for the β-pdf. The latter is particular evident at the origin, where the β-pdf leads to $P(Z/\langle Z\rangle) = 0$, as it can only take a value of zero or infinity. In contrast, the composite model completely reproduces $P(Z/\langle Z\rangle)$ for $Z/\langle Z\rangle = 0$. In Fig. 9 (x/d = 15), the T/NT interface contributes even more to the pdf and reflects the larger increase in the values of $P(Z/\langle Z\rangle)$ as Z approaches zero; note that the shape of $P(Z/\langle Z\rangle)$ is now bimodal with two maxima: one at $Z/\langle Z\rangle = 0$ and the other at $Z/\langle Z\rangle = 1.1$. With respect to the models, we observe similar trends as in Fig. 8; the composite model

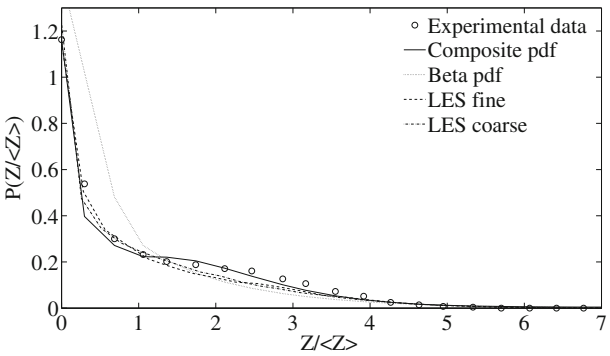

Fig. 10 Comparison of mixture fraction pdfs from LES, experiment and composite model at x/d = 15 and $\tilde{r} = 0.185$

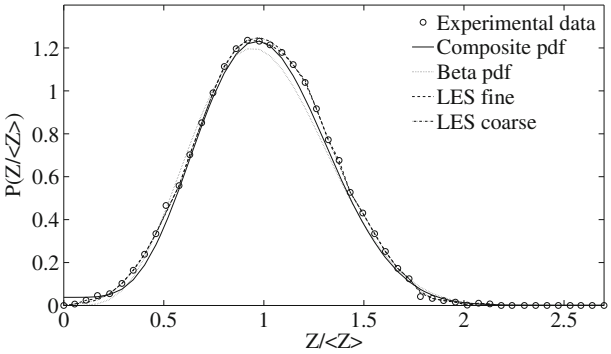

Fig. 11 Comparison of mixture fraction pdfs from LES, experiment and composite model at x/d = 20 and $\tilde{r} = 0$

reproduces both, value and location of the pdfs maximum as well as the non-zero value at the origin, where the β-pdf assumes $P(Z/\langle Z\rangle) = 0$. However, qualitatively the shape of the pdf is more or less reproduced by the β-pdf, while the two LES qualitatively and quantitatively differ significantly from the experimental data. Only the non-zero value at the origin is in close agreement with the experiment.

The increase in the T/NT interface contribution continues with radial distance and eventually, at larger radial distances, the T/NT interface layer contributions dominate $P(Z/\langle Z\rangle)$, as shown in Fig. 10 (x/d = 15). Again, the composite model shows an excellent agreement with the experimental data, while the β-pdf is only close to the measurements at large mixture fraction values and goes to infinity for $Z/\langle Z\rangle = 0$. At this highly intermittent location in the jet flow, the agreement between the two LES and the experiment, however, is excellent. The location corresponding to the pdf shown in Fig. 12 (x/d = 20, $\tilde{r} = 0.195$) is strongly intermittent. In contrast to the case shown in Fig. 10, the agreement between LES and experimental data is less satisfactory, as the LES data neither shows the slight intermediate plateau nor reaches the correct value of the pdf at $Z/\langle Z\rangle = 0$, which is overpredicted by the coarse and underpredicted by the fine LES.

Overall, we observe a good agreement between experimental and LES data. However, in particular at intermediate radial locations that are usually characterized by a bimodal pdf, deviations can be observed. This bimodal shape is due to a comparatively high contribution of the T/NT interface to the overall pdf. As this layer within

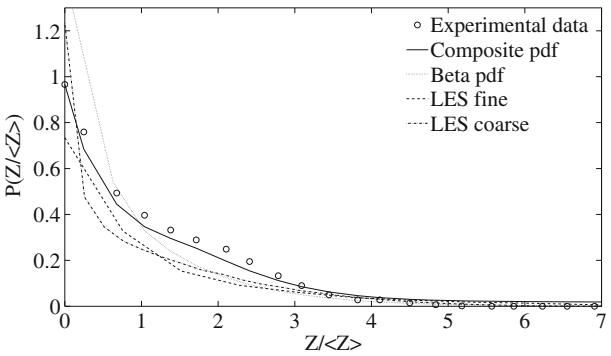

Fig. 12 Comparison of mixture fraction pdfs from LES, experiment and composite model at x/d = 20 and $\tilde{r} = 0.195$

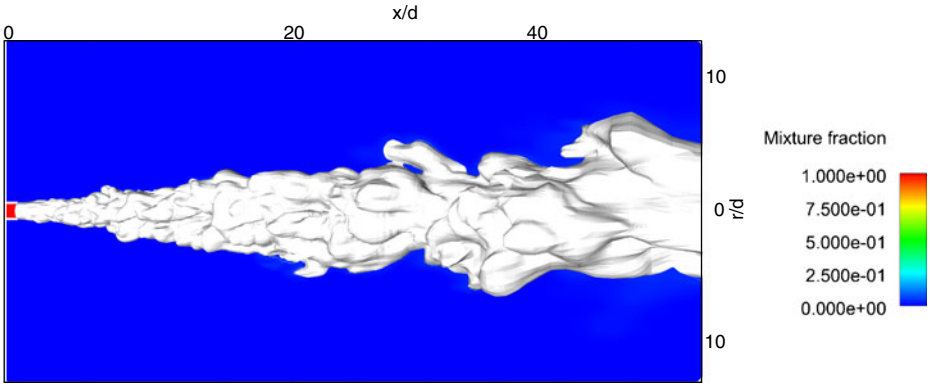

Fig. 13 Three-dimensional illustration of the instantaneous envelope iso-surface from the fine LES. For clarity only a small part of the domain is shown

the turbulent scalar field is dominated by diffusivity, we can thus conclude that the latter is not properly represented in the LES. With respect to the models, we observe a very good agreement between the measured and the composite model pdf, while the β-pdf exhibits significant deviations from the experimental data. Figures 9–12 clearly show that the composite model is well suited to reproduce $P(Z/\langle Z\rangle)$ even in the intermittent region of the flow, which is of major interest for modeling of non-premixed combustion. It is also noteworthy that we find considerable contributions from the T/NT interface layer even at highly turbulent regions of the flow.

4.2 Statistics of the scalar turbulent/non-turbulent interface layer

In order to investigate statistics of the interface layer, it first has to be detected in the scalar field. To this end, we follow a threshold procedure described by Prasad and Sreenivasan [52]. The threshold value at which the so called envelope, cf. [4],

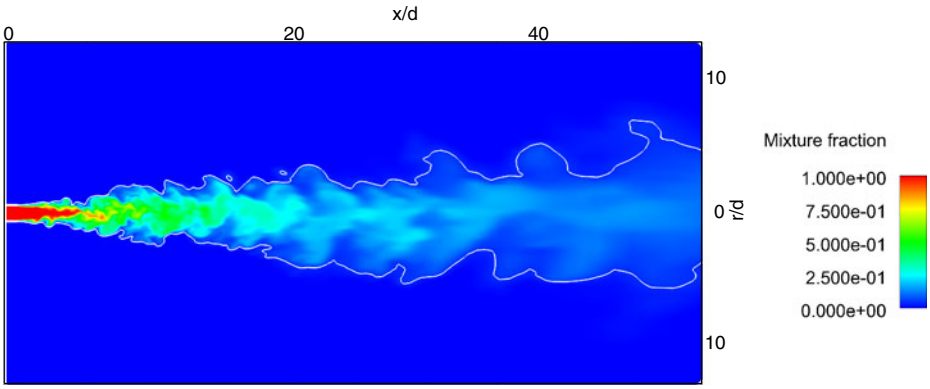

Fig. 14 Two-dimensional illustration of the instantaneous mixture fraction field and the instantaneous envelope contour for Fig. 13 from the fine LES. For clarity only a small part of the domain is shown

is located is determined as the local minimum value if the histogram of the mixture fraction within one planar image in the experiment or within the whole domain for the LES data is bimodal. In those cases, however, where the histogram is not bimodal, the average mixture fraction over the entire image is calculated as a function of the threshold using only those values that exceed this threshold. Then, the latter is simply calculated numerically by finding the inflection point of the threshold average mixture fraction curve. For the two LES this procedure yields a value of $Z = 0.05$ which is in good agreement with the experimental one ($Z = 0.045$), see Fig. 13 for an instantaneous mixture fraction field with a three-dimensional visualization of the envelope for the mixture fraction field that has been shown in Fig. 3. Figure 14 depicts the same instantaneous two-dimensional illustration of the envelope contour. In addition, the measurement locations from x/d = 10 to x/d = 30 are indicated by solid white lines to give a qualitative impression how the interface evolves downstream.

In section one, it has already been discussed that at the T/NT interface layer irrotational velocity fluctuations are usually found in the outer NT flow and that the velocity fluctuations change their character across the T/NT interface layer from vortical ($\boldsymbol{\omega}(= \nabla \times \mathbf{u})$ is non-zero) to irrotational ($\boldsymbol{\omega}$ is negligible), see [5]. In Fig. 14, we observe the fully turbulent region in the center part surrounded by outer fluid. Furthermore, a thin, more or less continuous and randomly moving interface layer is shown that is displayed by a solid white line and whose surface is of fractal character, cf. [53], see Fig. 13 for an illustration. The continuity of the interface layer is only disturbed by the separation of turbulent eddies from the main flow. These occasional patches are disconnected from the main jet body, due to the breaking away of vortical eddies—a physical process that is called detrainment and can also be observed in Figs. 13 and 14 at approximately x/d = 15 and x/d = 20. However, for free shear flows detrainment is a small effect, as such patches are usually re-entrained within a few eddy time scales, cf. [54]. If a scalar field is considered in the presence of a mean scalar gradient, there is usually a large increase of the scalar value observed across the T/NT interface layer, see for instance [4, 55].

In a next step, we compute the pdf of the radial location r_i of the T/NT interface layer normalized by the scalar half-width radius b_c, see Fig. 6a, to be consistent with previous works [2, 4]. The latter is shown in Fig. 15 for x/d = 30 from the two LES together with the experimental results and a Gaussian distribution. The mean radial

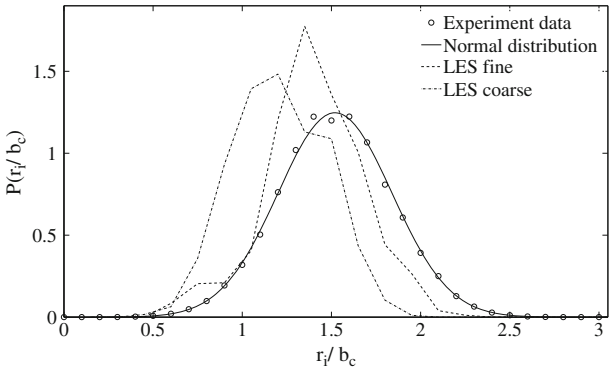

Fig. 15 Pdf $P(r_i/b_c)$ of the location of the T/NT interface layer for x/d = 30 from LES and experiment

location of the T/NT interface layer in the experiment is found at $\tilde{r} = 1.54 b_c$, and its most probable position is at $\tilde{r} = 1.49 b_c$, with the standard deviation σ of the pdf being $\sigma = 0.31 b_c$. These values are in good agreement with those of [4] for a turbulent round submerged liquid jet taken at $Re_0 = 2{,}000$ (note that in the experiment $b_c = 0.73 r_{1/2}$, where $r_{1/2}$ denotes the velocity half-width radius as obtained from LDA measurements).

The results for the two LES differ from these experimental results. While the fine LES is at least qualitatively close to the measurements, the coarse LES is far off. The fine LES has a maximum at $\tilde{r} = 1.35 b_c$ and the mean radial location of the T/NT interface layer is found at $\tilde{r} = 1.45 b_c$, which is thus approximately 6 % off. In contrast to this quite good agreement between experiment and fine LES, the maximum in the coarse LES is at $\tilde{r} = 1.20 b_c$ and the mean radial location of the T/NT interface layer is at $\tilde{r} = 1.27 b_c$ which deviates by almost 18 % from the experimental data.

Furthermore, we investigate the profile of the mean mixture fraction $\langle Z \rangle$ normalized by its centerline value Z_c in radial direction across the interface layer based on experimental and numerical data, shown in Fig. 16. A steep rise at $(r_i - r)/b_c = 0$ across the interface can be observed for the experimental data, in agreement with [4, 55]. This is followed by a small plateau, though the latter is not as pronounced as in [4], followed by a nearly linear increase with respect to the distance from the interface into the turbulent flow region.

This profile of the mixture fraction in radial direction across the interface layer is different when computed from the LES. In a first step, we notice that for both LES the mixture fraction profile in the outer flow region differs significantly from the experimental one as the mixture fraction value is not close to zero until right to the interface as the mixture fraction in both LES increases almost linearly from zero to $\langle Z \rangle / Z_c = 0.18$ in the zone in front of the interface layer up to $(r_i - r)/b_c = 1.1$. This trend is also present behind the T/NT interface though the agreement improves with increasing resolution. While the mixture fraction profile across the interface layer around $(r_i - r)/b_c = 0$ from LES is consistent with the measurements, the plateau and the following linear increase with respect to the distance from the interface layer into the turbulent flow region is not present in the coarse LES that directly behind the interface layer takes on much larger mixture fraction values and then asymptotically approaches the experimental values. In contrast, the fine LES follows the measurements much closer. Although this simulation also overpredicts

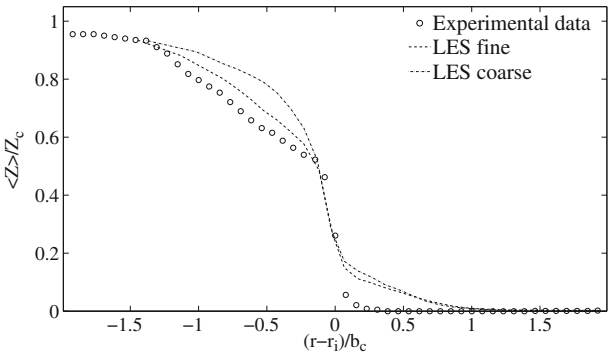

Fig. 16 Comparison of the profiles of the conditional mean mixture fraction across the T/NT interface layer for x/d = 30 from LES and experiment

the mixture fraction on the turbulent side of the interface, the linear increase is reproduced much better than in the coarse LES.

In summary, we observe that the sharp jump of the mixture fraction across the interface that is reported for the experimental study [2] is not as distinct in the LES results, but rather diffused in radial direction. We therefore conclude that two effects contribute to these deviations. On the one hand, we observe effects stemming from a lack of resolution at $(r_i - r)/b_c = 0$. As discussed in section one, the T/NT interface thickness scales with the Taylor microscale so that this layer in the flow strongly depends on the grid. On the other hand, the deviations of the mixture fraction profiles in direction of the fully turbulent and in particular in the outer flow region, respectively, are attributed to model effects, more specifically to a failure of the applied sub-grid model in this region of the flow. Consequently, either a high resolution is necessary to properly reproduce statistics of the T/NT interface layer or additional models have to be included in LES to account for the above discussed deficiencies.

5 Conclusion

This study has investigated the scalar T/NT interface layer in the mixture fraction field of a turbulent round propane jet with coflowing carbon dioxide at a nozzle based Reynolds number $Re_0 = 8{,}610$. To this end, two LES with different resolutions of 1.5 million grid cells and 3.1 million grid cells, respectively, have been performed and were compared to experimental results that were obtained via high frequency two-dimensional Rayleigh scattering measurements of the mixture fraction at downstream diameters between x/d = 10 and x/d = 30, cf. [1, 2] (Gampert et al. 2013, Scalar gradient trajectory measurements using high-frequency cinematographic planar rayleigh scattering, submitted).

In a first step, the LES has been validated based on the experimental data and a very good agreement is observed for the axial decay along the centerline of the velocity and the mixture fraction as well as for radial profiles of the mean and r.m.s. values of these quantities. Afterwards, the mixture fraction pdf has been examined at various axial and radial positions in the jet flow. Overall, a good agreement between numerical and experimental data was observed. However, in the flow region where the contributions of the T/NT interface layer to the pdf are dominant and the latter has a (close to) bimodal shape, cf. [36], large discrepancies were observed especially for the coarse grid that are absent on the centerline and in the highly intermittent outer region.

In a next step, statistics of the T/NT interface layer have been studied, where a satisfactory agreement for the pdf of the location of the envelope that is embedded at the outer end of the interface layer from the fine LES with the experimental data was observed, while the one with the coarse grid exhibited considerable deviations. Finally, the mixture fraction profile across the interface has been investigated where the same trend as for the pdf of the location was present. In particular, it has been found that the sharp jump of the scalar value across the interface that was reported for the experimental study [2] is less distinct in the LES results, but rather diffused in radial direction, a finding that was supported by the investigation of instantaneous visualizations of the mixture fraction field together with the envelope.

Acknowledgements MG and NP thank the NRW-Research School "BrenaRo" and the Cluster of Excellence "Tailor-Made Fuels from Biomass", which is funded by the Excellence Initiative of the German federal state governments to promote science and research at German universities. KK and HP acknowledge the support of the collaborative research center SFB 686, which is funded by the German Research Association (Deutsche Forschungsgemeinschaft (DFG)). This support is gratefully acknowledged. Computer resources for this project have been provided by the Jülich Aachen Research Alliance (JARA) under grant jara0009.

References

1. Gampert, M., Schaefer, P., Narayanaswamy, V., Peters, N.: Gradient trajectory analysis in a jet flow for turbulent combustion modelling. J. Turbul. (2012). doi:10.1080/14685248.2012.747688
2. Gampert, M., Narayanaswamy, V., Schaefer, P., Peters, N.: Superlayer contributions to the mixture fraction Pdf in a turbulent round jet flow. J. Fluid Mech. (2013, in press)
3. Gampert, M., Schaefer, P., Peters, N.: Experimental investigation of dissipation element statistics in scalar fields of a jet flow. J. Fluid Mech. **724**, 337–366 (2013)
4. Westerweel, J., Fukushima, C., Pedersen, J.M., Hunt, J.C.R.: Momentum and scalar transport at the turbulent/non-turbulent interface of a jet. J. Fluid Mech. **631**, 199–230 (2009)
5. Bisset, D.K., Hunt, J.C.R., Rogers, M.M.: The turbulent/non-turbulent interface bounding a far wake. J. Fluid Mech. **451**, 383–410 (2002)
6. Philip, J., Marusic, I.: Large-scale eddies and their role in entrainment in turbulent jets and wakes. Phys. Fluids **24**(5), 055108 (2012)
7. Monin, A.S., Yaglom, A.M.: Statistical Fluid Mechanics. MIT Press (1975)
8. Townsend, A.A.: The Structure of Turbulent Shear Flow. Cambridge University Press (1956)
9. Townsend, A.A.: Local isotropy in the turbulent wake of a cylinder. Austral. J. Sci. Res. **A1**, 161–174 (1948)
10. Townsend, A.A.: The fully developed turbulent wake of a circular cylinder. Austral. J. Sci. Res. **A2**, 451–468 (1949)
11. Corrsin, S., Kistler, A.L.: Free-Stream Boundaries of Turbulent Flows, vol. 1244. NACA Report (1955)
12. Kline, S.J., Reynolds, W.C., Schraub, F.A., Runstadler, P.W.: The structure of turbulent boundary layers. J. Fluid Mech. **30**, 741–773 (1967)
13. Brown, G.L., Roshko, A.: On density effects and large structure in turbulent mixing layers. J. Fluid Mech. **64**, 775–816 (1974)
14. Dimotakis, P.E., Miake-Lye, R.C., Papantoniou, D.A.: Structure and dynamics of round turbulent jets. Phys. Fluids **26**, 3185–3192 (1983)
15. Liepmann, D., Gharib, M.: The role of streamwise vorticity in the near-field entrainment of round jets. J. Fluid Mech. **245**, 643–668 (1992)
16. Cannon, S., Champagne, E., Glezer, A.: Observations of large-scale structures in wakes behind axisymmetric bodies. Exp. Fluids **14**, 447–450 (1993)
17. Townsend, A.A.: The mechanism of entrainment in free turbulent flows. J. Fluid Mech. **26**, 689–715 (1966)
18. Townsend, A.A.: Organized eddy structures in turbulent flows. PCH, PhysicoChem. Hydrodyn. **8**(1), 23–30 (1987)
19. Grant, H.L.: The large eddies of turbulent motion. J. Fluid Mech. **4**, 149–190 (1958)
20. Marusic, I., Adrian, R.A.: Scaling issues and the role of organized motion in wall turbulence. In: Davidson, P., Kaneda, Y., Sreenivasan, K.R. (eds.) Ten Chapters in Turbulence. Cambridge University Press, Cambridge (2013)
21. Perry, A.E., Chong, M.S.: On the mechanism of wall turbulence. J. Fluid Mech. **119**, 173–217 (1982)
22. Nickels, T.B., Perry, A.E.: An experimental and theoretical study of the turbulent coflowing jet. J. Fluid Mech. **309**, 157–182 (1996)
23. Marusic, I., Perry, A.E.: A wall-wake model for the turbulence structure of boundary layers. Part 2. Further experimental support. J. Fluid Mech. **298**, 389–407 (1995)
24. Yoda, M., Hesselink, L., Mungal, M.G.: Instantaneous three-dimensional concentration measurements in the self-similar region of a round high-Schmidt-number jet. J. Fluid Mech. **279**, 313–350 (1994)

25. Westerweel, J., Fukushima, C., Pedersen, J.M., Hunt, J.C.R.: Mechanics of the turbulent nonturbulent interface of a jet. Phys. Rev. Lett. **95**, 174501 (2005)
26. Mathew, J., Basu, A.J.: Some characteristics of entrainment at a cylindrical turbulence boundary. Phys. Fluids **14**, 2065–2072 (2002)
27. Hunt, J.C.R., Eames, I., da Silva, C.B., Westerweel, J.: Interfaces and inhomogeneous turbulence. Philos. Trans. R. Soc. Lond. A **369**, 811–832 (2011)
28. Westerweel, J., Hofmann, T., Fukushima, C., Hunt, J.C.R.: The turbulent/non-turbulent interface at the outer boundary of a self-similar turbulent jet. Exp. Fluids **33**, 873–878 (2002)
29. Holzner, M., Liberzon, A., Nikitin, N., Kinzelbach, W., Tsinober, A.: Small-scale aspects of flows in proximity of the turbulent/non-turbulent interface. Phys. Fluids **19**(7), 071702 (2007)
30. Holzner, M., Luethi, B., Tsinober, A., Kinzelbach, W.: Acceleration, pressure and related quantities in the proximity of the turbulent/non-turbulent interface. J. Fluid Mech. **639**, 153–165 (2007)
31. da Silva, C.B., Pereira, J.C.: Invariants of the velocity-gradient, rate-of-strain, and rate-of-rotation tensors across the turbulent/nonturbulent interface in jets. Phys. Fluids **20**, 055101 (2008)
32. da Silva, C.B., Pereira, J.C.: The role of coherent vortices near the turbulent/non-turbulent interface in a planar jet. Phil. Trans. R. Soc. A **369**, 738–753 (2011)
33. da Silva, C.B., Taveira, R.R.: The thickness of the turbulent/nonturbulent interface is equal to the radius of the large vorticity structures near the edge of the shear layer. Phys. Fluids **22**, 121702 (2010)
34. Westerweel, J., Petracci, A., Delfos, R., Hunt, J.C.R.: Characteristics of the turbulent/non-turbulent interface of a non-isothermal jet. Phil. Trans. R. Soc. A **369**, 723–737 (2011)
35. Holzner, M., Liberzon, A., Nikitin, N., Lüthi, B., Kinzelbach, W., Tsinober, A.: A Lagrangian investigation of the small scale features of turbulent entrainment through 3D-PTV and DNS. J. Fluid Mech. **598**, 465–475 (2008)
36. Effelsberg, E., Peters, N.: A composite model for the conserved scalar PDF. Combust. Flame **50**, 351–360 (1983)
37. Mellado, J.P., Wang, L., Peters, N.: Gradient trajectory analysis of a scalar field with internal intermittency. J. Fluid Mech. **626**, 333–365 (2009)
38. Desjardins, O., Blanquart, G., Balarac, G., Pitsch, H.: High order conservative finite difference scheme for variable density low Mach number turbulent flows. J. Comput. Phys. **227**, 7125–7159 (2008)
39. Meneveau, C., Lund, T.S., Cabot, W.H.: A Lagrangian dynamic subgrid-scale model of turbulence. J. Fluid Mech. **319**, 353–385 (1996)
40. Meneveau, C., Katz, J.: Scale-invariance and turbulence models for large-eddy simulation. Annu. Rev. Fluid Mech. **32**, 1–32 (2000)
41. Knudsen, E., Pitsch, H.: A dynamic model for the turbulent burning velocity for large eddy simulation of premixed combustion. Combust. Flame **154**(4), 740–760 (2008)
42. Falgout, R., Yang, U.: A library of high performance preconditioners. In: Lecture Notes in Computer Science, vol. 2331. Springer, Berlin Heidelberg (2002)
43. Pierce, C.D., Moin, P.: A dynamic model for subgrid-scale variance and dissipation rate of a conserved scalar. Phys. Fluids **10**, 3041–3044 (1998)
44. Jiang, G.S., Peng, D.: Weighted ENO schems for Hamilton-Jacobi equations. J. Sci. Comput. **21**(6), 2126–2143 (2000)
45. Pope, S.B.: Turbulent Flows. Cambridge University Press (2000)
46. Talbot, B., Mazellier, N., Renou, B., Danaila, L., Boukhalfa, M.: Time-resolved velocity and concentration measurements in variable-viscosity turbulent jet flow. Exp. Fluids **47**, 769–787 (2009)
47. Amielh, M., Djeridane, T., Anselmet, F., Fulachier, L.: Velocity near-field of variable density turbulent jets. Int. J. Heat Mass Transfer **39**(10), 2149–2164 (1996)
48. Lubbers, C.L., Brethouwer, G., Boersma, B.J.: Simulation of the mixing of a passive scalar in a round turbulent jet. Fluid Dyn. Res. **28**(3), 189–208 (2001)
49. Panchapakesan, N.R., Lumley, J.L.: Turbulence measurements in axisymmetric jets of air and helium. Part 1. Air jet. J. Fluid Mech. **246**, 197–223 (1993)
50. Richards, C.D., Pitts, W.M.: Global density effects on the self-preservation behaviour of turbulent free jets. J. Fluid Mech. **254**, 417–435 (1993)
51. Schefer, R.W., Dibble, R.W.: Rayleigh scattering measurements of mixture fraction in a turbulent nonreacting propane jet. AIAA J. **23**(7), 1070–1078 (1986)

52. Prasad, R.R., Sreenivasan, K.R.: Scalar interfaces in digital images of turbulent flows. Exp. Fluids **7**, 259–264 (1989)
53. Sreenivasan, K.R., Meneveau, C.: The fractal facets of turbulence. J. Fluid Mech. **173**, 357–386 (1986)
54. Hussain, A.K.M.F., Clark, A.R.: On the coherent structure of the axisymmetric mixing layer: a flow-visualization study. J. Fluid Mech. **104**, 263–294 (1981)
55. Alexopoulos, C.C., Keffer, J.F.: Turbulent wake in a passively stratified field. Phys. Fluids **14**, 216–224 (1971)